Chemical Engineering Journal 471 (2023) 144448

Contents lists available at ScienceDirect

Chemical Engineering Journal

journal homepage: www.elsevier.com/locate/cej

Triggering electrode multi-catalytic activity for reversible symmetric solid oxide cells by Pt-doping lanthanum strontium ferrite

Anna Paola Panunzi [a], Leonardo Duranti [a,*], Igor Luisetto [b], Nicola Lisi [b], Marcello Marelli [c], Elisabetta Di Bartolomeo [a]

[a] Department of Chemical Science and Technologies, University of Rome Tor Vergata, Via della Ricerca Scientifica, 00133 Rome, Italy
[b] ENEA C.R. Casaccia, Via Anguillarese 301, 0123 S.M. di Galeria, Roma, Italy
[c] CNR SCITEC - Istituto di Scienze e Tecnologie Chimiche "Giulio Natta", Via Fantoli 16/15, 20138 Milano, Italy

ARTICLE INFO

Keywords:
Reversible Solid Oxide Cells
Symmetric Cells
Perovskite oxides
Platinum doping
Exsolution

ABSTRACT

Among the up-and-coming technologies, reversible solid oxide cells (r-SOCs) represent a highly efficient way to store and convert energy using a single device. The interchangeability between SOFC and SOEC operation is the key aspect, though for its technological advancement the development of performing, versatile and robust electrodes must be pursued. A multi-purpose catalyst would allow for the design of a reversible symmetric cell (r-SSOC), greatly reducing fabrication and maintenance costs. However, such a flexible electrode material must comply with the requirements of both SOC electrodes, namely ensuring high performance in a wide pO_2 range: catalytic activity towards fuel oxidation and H_2O/CO_2 reduction, electronic and ionic conductivity, long-term stability, tolerance to carbon deposition. In this work, platinum doping at the B-site of a lanthanum strontium ferrite (LSFPt) endowed the parent perovskite with superior versatility, making it able to operate as oxygen exchange catalyst as well as fuel electrode material. 5-mol% Pt inclusion enhanced the ORR/OER activity, lowering the LSF area-specific resistance by 29% and approaching the state-of-the-art LSCF performance. After reduction, Pt-Fe finely distributed exsolution provided the fuel electrode with catalytically active sites. LSFPt-symmetric H_2-SOFCs and CO_2-SOECs, displayed 720 $mW \bullet cm^{-2}$ power density and 1.66 $A \cdot cm^{-2}$ current density at 1.6 V, respectively, at 850 °C. Endurance tests on LSFPt-based r-SSOCs demonstrated a remarkably stable SOFC/SOEC cyclability and a steady current density output for over 370 h in 50:50 CO_2:CO at 850 °C.

1. Introduction

The intermittent and seasonal nature of renewables requires efficient systems, capable of storing excess energy and supplying it during consumption peaks. Among innovative technologies, reversible solid oxide cells (r-SOCs) combine the concepts of solid oxide electrolyser cell (SOEC) and solid oxide fuel cell (SOFC) in a single device. R-SOCs can alternatively switch between power-to-fuel mode (turning energy into storable fuels) and fuel-to-power mode (converting back the stored fuels into electrical energy) with high intrinsic efficiency resulting from high-temperature operation [1,2].

The conventional device architecture Ni-YSZ|YSZ|LSM set the standards for H_2/H_2O operation as both fuel and electrolysis cells. Nevertheless, state-of-the-art materials display operational shortcomings that restrict the application of commercial devices to a limited, high-temperature range, and to highly purified gas feeds. For instance, the established air electrode material, LSM, suffers from poor activity in the intermediate temperature range, mainly due to its intrinsic negligible ionic conductivity [3]. Moreover, LSM showed degradation under cell polarizations, both cathodic (SOFC) and anodic (SOEC) [4]. On the other side of the cell, the composite Ni-YSZ fuel electrode shows a series of weaknesses when it comes to fuel flexibility, one of the distinctive features of solid oxide cells. Ni-YSZ has low tolerance to fuel impurities (H_2S) [5] and its catalytic activity rapidly degrades in presence of carbon-containing species. This latter issue impairs Ni-YSZ utilization in hydrocarbons-fuelled fuel cells, due to coking [6] but also in CO_2-based electrolysers, due to progressive carbon deposition [7]. The cermet nature of Ni-YSZ suffers from limited TPB extension [8] and instability over prolonged operation under polarization [4]. Moreover, the fuel electrode usually plays the role of mechanical cell support, and nickel volume variations over redox cycles expose the whole cell to mechanical failure risk [9].

* Corresponding author.
E-mail address: leonardo.duranti@uniroma2.it (L. Duranti).

https://doi.org/10.1016/j.cej.2023.144448
Received 10 March 2023; Received in revised form 15 June 2023; Accepted 26 June 2023
Available online 28 June 2023

The pursuit of newly-designed materials has recently been oriented towards the tailoring of a multi-purpose catalyst, both for anodic and cathodic applications. To this extent, the concept of symmetric solid oxide cells (SSOCs) minimizes mechanical and thermo-chemical affinity issues to a single type of electrode/electrolyte interface, reducing fabrication/maintenance costs and favouring large-scale production [10,11]. Additionally, the effort of designing a catalyst able to withstand antipodal pO_2 conditions at high temperature can be pushed forward, towards the optimization of a symmetric *and* reversible solid oxide cell (r-SSOC) [12]. Together with redox resistance, the electrode material of a r-SSOC must ensure both mixed ionic-electronic conductivity and versatile activity towards all the reactions involved: ORR, OER, oxidation of various fuels and H_2O/CO_2 reduction. Low cost, earth-abundant iron-based perovskite oxides represent the ideal candidates as multi-tasking electrode materials [13,14]. These compounds benefit from highly versatile Fe redox chemistry, which is responsible for their intrinsic MIEC nature, and provides high structural tolerance to non-stoichiometry and Fe replacement. In particular, B-site substitution on Sr-doped lanthanum ferrites $La_{1-x}Sr_xFe_{1-y}M_yO_{3\pm\delta}$ has been extensively explored, aiming at increasing structural stability under highly reducing environments (M = Ti, Cr, Mn) [15–17], or electronic/ionic conductivity and catalytic activity (M = Co, Ni, Cu) [18,19].

20 mol% Co-substitution on LSF (LSCF) represented a breakthrough for outstanding performance in the intermediate temperature range (600–800C°). Nevertheless, LSCF shows poor stability upon long-time operation, due to solid state reactions with the electrolyte, Sr segregation, and Co migration [20]. Moreover, the economic and ethical implications of cobalt use in the field of green energy must be considered: Co demand, in fact, is expected to witness a five-fold growth in few decades mainly due to the future market of electric vehicles [21]. As an alternative to cobalt utilization, a valuable solution in terms of electrocatalytic performance is the partial substitution of B-site iron with a small amount (<5 mol%) of platinum group metals (PGMs). Such quantities of PGMs can be profitably harvested from secondary sources, such as spent automotive three-way catalysts (TWCs) [22] or, more recently, from electrode membrane for hydrogen production [23]. Recycling is an economically and ecologically convenient PGMs source, an alternative to localized low-grade ores extraction. PGM-doped perovskite oxides are reduced to their metallic state displaying largely favourable Gibbs free energy [24], thus when doped into complex oxide structures, they can easily segregate to the oxide surface upon high-temperature reduction. This PGMs segregation in form of metallic nanoparticles, alone or alloyed with Fe, is known as *exsolution*, and promotes catalytic activity for fuel oxidation [25–28]. Pt inclusion within a stable lanthanum titanate has been achieved through solid-state reaction, avoiding thermal decomposition of platinum oxide precursors, to obtain a stable catalyst for CO oxidation and other fuels conversion [28]. Lately, 1.5 at% Pt was doped into an LSF thin film grown by pulsed laser deposition. A multi layered structure was used as a model electrode to study how Pt surface doping lowered the electrode polarization resistance [29].

Here, 5 mol% Pt was successfully doped at the B-site of $La_{0.6}Sr_{0.4}FeO_{3-\delta}$ through citrate-solution combustion method. The effect of Pt-doping on the parent perovskite structure was evaluated by X-ray powder diffraction (XPRD), X-ray photoelectron spectroscopy (XPS), thermogravimetric analysis (TG) and oxygen temperature-programmed desorption (O_2-TPD). $La_{0.6}Sr_{0.4}Fe_{0.95}Pt_{0.05}O_{3-\delta}$ (LSFPt) performance as a SOC air electrode was evaluated in terms of electrical conductivity and polarization resistance as a function of temperature and pO_2. The rate-limiting steps of oxygen exchange reactions were investigated by means of equivalent circuit modelling (EC) and distribution of relaxation times (DRT) on electrochemical impedance spectroscopy (EIS) obtained data. Results are compared to both the undoped parent perovskite (LSF) and to a commercially available state-of-the-art 20 mol% Co doped (LSCF). LSFPt structural evolution after thermal treatment in 5% H_2/Ar was screened by means of XRPD, temperature-programmed reduction (H_2-TPR), transmission electron microscopy (TEM) and scanning electron microscopy (FE-SEM) coupled with elemental analysis (EDX) to assess its applicability as a fuel electrode as well. Finally, LSGM-based symmetric cells were tested as H_2-SOFCs, CO_2-SOECs, and r-SOCs assessing long-term (over 370 h) stability and reversibility.

2. Experimental

2.1. Samples preparation

$La_{0.6}Sr_{0.4}FeO_{3-\delta}$ (LSF) and $La_{0.6}Sr_{0.4}Fe_{0.95}Pt_{0.05}O_{3-\delta}$ (LSFPt) were synthesized by citrate–nitrate solution combustion method. Stoichiometric amounts of precursors, such as: $La(NO_3)_3{\cdot}6H_2O$ (Alfa Aesar©, 99.999%), $Sr(NO_3)_2$ (Aldrich®, 99.995%), $Fe(NO_3)_3{\cdot}9H_2O$ (Aldrich®, 99.99+%) and $H_{12}N_6O_6Pt$ (Alfa Aesar©, 99.995%) were dissolved in a distilled water solution (0.1 M) on a hot plate. Acting as fuel and complexing agent, citric acid (CA) was added in 1:1 CA/ions molar ratio. The pH of the solution was adjusted to 6.5 by dropwise addition of NH_3(aq). The solution was slowly dehydrated to obtain a gel, then the combustion was ignited by raising the plate temperature up to 350 °C. The obtained ashes were milled and homogenized. To maximize the perovskite catalyst surface area, the lowest possible calcination temperature was chosen, after the complete loss of excess water, nitrates and carbonates. The calcination temperature was set at 750 °C as resulting from thermogravimetric analysis performed on the post-combustion sample (Fig. S1 - Supplementary Material). Ashes were calcined at 750 °C for 3 h. The obtained oxide powder was grounded in an agate mortar and calcined again to ease the formation of a pure phase. Commercial (*Praxair)* $La_{0.6}Sr_{0.4}Fe_{0.8}Co_{0.2}O_{3-\delta}$ (LSCF) was used as a reference air electrode material.

2.2. Instrumental characterizations

Specific surface area was assessed applying the Brunauer-Emmett-Teller method (BET) in the linear 0.03 ÷ 0.3 span of relative pressure (p/p^0). N_2 adsorption/desorption isotherms were acquired at −196 °C by means of a Micromeritics Tristar II Plus Surface Area and Pore Size Analyzer. Samples were subjected to a degassing step in vacuum at 350 °C for 4 h before analysis.

X-ray powder diffraction (XRPD) analyses were performed using a Philips X-Pert Pro 500 diffractometer with Cu Kα radiation (λ = 1.54056 Å) in the range 2θ = 20° −90° with 0.015° step size and 10 s time per step. The mean crystallite size was calculated using the Scherrer equation and the broadening of the most intense XRPD peak.

Thermogravimetric measurements were carried out under nitrogen flux using a TG-DSC 1 (Mettler Toledo, STAR system). The mass loss was recorded between 50 °C and 1000 °C, with a heating ramp (5 °C·min^{-1}). Prior to each analysis, the sample (~30 mg) was loaded in a Pt crucible and pre-heated in air up to 500 °C (5 °C·min^{-1}) to ease adsorbed contaminants desorption, then cooled to room temperature. Buoyancy effect was subtracted. XRPD analyses were performed on the samples before and after the TG measurements.

Oxygen temperature programmed desorption (O_2-TPD) and hydrogen temperature programmed reduction (H_2-TPR) were performed with an AutoChem 2950 HP Micromeritics automated flow-through device with a TCD detector. To favour the desorption of adsorbed exogenous species, the samples were treated 1 h at 350 °C in 5% O_2/He gas mixture (30 cm^3·min^{-1}) then cooled down to 50 °C in this controlled environment. O_2-TPD measurements, were carried out in flowing He (30 cm^3·min^{-1}), and oxygen released by the samples was monitored between 50 °C and 850 °C (10 °C ·min^{-1}). H_2-TPR analyses were performed flowing 30 cm^3·min^{-1} of 5% H_2/Ar gas mixture in the reactor, following the same thermal ramp used for O_2-TPD experiments, this time up to 1000 °C. A TCD detector recorded H_2 consumption. CuO (99.99%, Aldrich®) was reduced for TCD calibration. XRPD analyses were performed on the samples before and after the O_2-TPD

measurements.

X-ray photoemission spectroscopy (XPS) was performed on dense perovskite oxide samples. Sintered disks were obtained by mixing the perovskite powders with 5% of organic binder (PVP), uniaxially pressing the mixture at 260 MPa and sintering the obtained disks at 1250 °C (2 °C·min^{-1}) for 4 h. XPS core level spectra were acquired with Al Kα X-ray radiation at 1.486 eV (VG Escalab MkII Spectrometer).

LSF and LSFPt sintered samples were also treated with oxygen plasma (30 min, 100 W, Diener Electronic, model Zepto), then exposed to flowing air for 10 min and XPS spectra acquisition was repeated, to enhance the adsorbed molecular oxygen contribution in O 1 s signal.

Morphological analyses were performed using a Zeiss Leo SUPRA™ 35 field emission scanning electron microscope (FE-SEM), Transmission Electron Microscope (TEM) and Scanning Transmission Electron Microscope (STEM). For TEM analyses, specimens were gently ground in an agate mortar, suspended in isopropyl alcohol, and placed for 10 min in an ultrasound bath. A suspension drop was deposited onto a lacey carbon copper TEM grid and analysed after overnight drying. The grid was inserted in the column of a ZEISS LIBRA200FE electron microscope for imaging and analysis. EDX (Energy Dispersive X-ray Analysis) map and line profiles were performed in STEM mode, with an OXFORD (X-stream 2) probe.

Electrical conductivity was measured using the direct current four-point probe technique on sintered samples. The same sintering procedure previously described for XPS sample preparation was followed. Au current collectors were used. Conductivity measurements were performed under air flux (100 cm^3·min^{-1}) in the 200 °C–850 °C temperature range.

2.3. Cells configuration

The electrolyte-supported configuration was chosen for the electrochemical characterization of symmetric cells. $La_{0.8}Sr_{0.2}Ga_{0.8}Mg_{0.2}O_{3-\delta}$ (LSGM, purchased by *Praxair*) was mixed with 5% of PVP, pressed at 370 MPa and sintered 10 h at 1500 °C (2 °C·min^{-1}). Dense pellets (diameter 10 mm, thickness 300 μm) were obtained.

Inks for electrode deposition were prepared by mixing the selected perovskite powder with serigraphic terpineol-based oil (purchesed by *Fuelcellmaterials*). The fuel electrode was spin-coated on one side of LSGM electrolyte, while the air electrode was deposited on the other side via brush painting. A thermal treatment (2 h at 1100 °C, 5 °C·min^{-1}) ensured adequate adhesion of the electrodes to the electrolyte. The thickness of the fuel electrode was 60 μm while the air electrode was 30 μm-thick. The air electrode area was used for data normalization. An Au adhesive paste (T10112, Metalor Technologies Ltd., U.K.) and gold wires (Au 99.99%) were used as current collectors. Thus obtained symmetric cells will be named X/LSGM/X with X = LSFPt, LSF, LSCF in the following.

Area-specific resistance (ASR) was measured performing electrochemical impedance spectroscopy (EIS) measurements on symmetric cells, by means of a frequency response analyser (FRA, Solartron 1260) coupled with a dielectric interface (Solartron 1296). EIS spectra were acquired in the 0.01 Hz−2 MHz frequency range, with a set AC voltage amplitude of 10 mV. ASR was evaluated vs. temperature (550 °C−800 °C) and vs. oxygen partial pressure (0.01 atm−0.21 atm) at constant temperature (750 °C). The different pO_2 environments were obtained diluting air with Ar. Impedance data were fitted with equivalent circuit modelling (using ZSimpWin software). The distribution of relaxation times (DRT) method was also used to investigate the trend of the single reaction steps occurring at the electrode. DRT analysis was carried out using a program developed by Ciucci et al. [30] running on MATLAB.

SOFC, SOEC and r-SOC tests were performed on symmetric cells. Samples were sealed on an alumina-based cell station using commercial ceramic paste (Aremco Ceramabond 552). The electrochemical cell characterizations (I-V characteristics, EIS analyses, potentiostatic tests for cell stability evaluation) were recorded with a PARSTAT 4000A potentiostat·galvanostat/EIS analyzer. EIS spectra (frequency range 0.01 Hz−10 MHz, AC signal 10 mV) were acquired at open circuit voltage (OCV) and at various cell voltages. Impedance data were fitted and deconvoluted as reported above. SOFC tests were run at 650 °C, 750 °C and 850 °C, fluxing 100 cm^3·min^{-1} H_2 at the fuel electrode. SOEC tests were performed at 850 °C fluxing 100 cm^3·min^{-1} of pure CO_2 at the fuel electrode. Cell reversibility (r-SOC) was assessed at 850 °C fluxing 50% CO_2 and 50% CO over time. The air-electrode was exposed to static air in SOFC, SOEC and r-SOC tests.

3. Results and discussion

3.1. Samples characterization

Fig. 1a shows the XRPD diffractograms of LSF and LSFPt samples after calcination. Both stoichiometries show the characteristic $La_{0.6}Sr_{0.4}FeO_{3-\delta}$ (JCPDS 82-1961) rhombohedral structure belonging to the R $\overline{3}$ c space group. As reported in the $31° < 2\theta < 34°$ enlargement in Fig. 1a, the main peak position is centred at $2\theta = 32.54°$ and 32.40° for LSF and LSFPt, respectively. Pt-doping shifted the LSF pattern toward lower angles, indicating a lattice expansion resulting from the substitution of Fe^{3+}/Fe^{4+} ions (0.645/0.584 Å) with larger Pt^{2+}/Pt^{4+} ions (0.800/0.625 Å) into the lattice [31]. The change in crystallite size upon Pt-doping was calculated from the Scherrer formula applied using the FWHM of the most intense peaks. The presence of 5 mol% Pt reduced the crystallite size from 29 ± 1 nm for LSF to 25 ± 1 nm. The surface area values calculated with the Brunauer-Emmett-Teller method on the adsorption branch of the N_2 adsorption/desorption isotherms (Fig. S2), showed comparable surface areas for LSFPt and LSF, 12.18 ± 0.04 m^2·g^{-1} and 10.56 ± 0.04 m^2·g^{-1}, respectively. 5 mol% Pt replacement at the B-site introduced a short-range perturbation in LSF crystalline structure, reducing the mean crystallite size. The lattice distortion percentage ε [32] was estimated according to

$$\varepsilon = \frac{\beta}{4tan[\theta]}$$

A larger ε was obtained for LSFPt (0.0052%) as compared to LSF (0.0045%).

Fig. 1b shows Pt 4f XPS spectrum obtained from LSFPt. Two main peaks related to Pt $4f_{7/2}$ and Pt $4f_{5/2}$ are revealed, at 73.3 eV and 76.5 eV, respectively. According to the literature, each set of peaks can be deconvoluted into two components, belonging to Pt^{2+} and Pt^{4+} species. The former contributions usually appear around 72.5 eV and 76 eV, while the latter at 74 eV and 77 eV [29,33]. No relevant fraction of metallic platinum (main peak around 71 eV) [34] can be seen in Fig. 1b and from the XPS data fitting. The analysis of the relative concentrations revealed that most of the doping platinum is coordinated in its highest oxidation state, Pt^{4+}, that accounted for 74.7%, with the remaining 25.3% being Pt^{2+}.

Fig. 1c shows the comparison of the Fe 2p spectra of LSF and LSFPt. The asymmetric feature of the spectra is characteristic of B-site iron in lanthanum ferrites: two double-peaks, related to Fe $2p_{3/2}$ (710 eV) and Fe $2p_{1/2}$ (726 eV) together with two broad satellites at 720 eV and 734 eV. The peaks around 710 eV and 724 eV can be attributed to Fe^{3+}, while the enhanced features around 713 eV and 726 eV have been associated with Fe^{4+} species [35–37]. According to these recent findings, here Fe 2p spectra were fitted with two components, the first clearly attributed to Fe^{3+} [38] and the second, appearing as a shoulder at higher binding energies, to the presence of varying amounts of the Fe^{4+} superoxide. Thus, iron cations are mainly present as Fe^{3+} and Fe^{4+} with the relative amounts listed in Table 1. The presence of a minor quantity of Fe^{2+} associated to structural defects cannot be excluded, yet since the XPS measurements were performed on as prepared (oxidized) samples, the peak related to Fe^{2+} presence (~708 eV for $2p_{3/2}$ signal [39]) cannot be

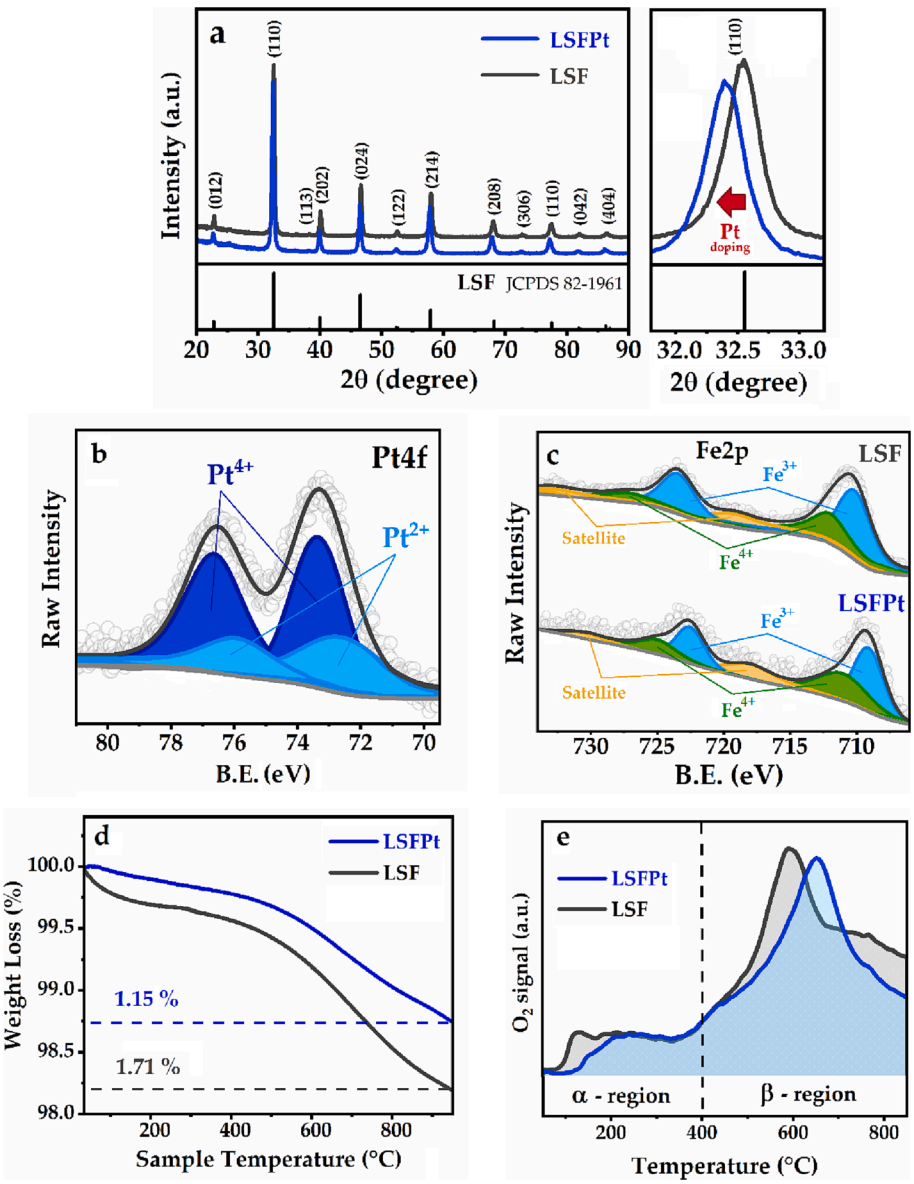

Fig. 1. a) left: XRPD patterns of LSF and LSFPt powders; right: $31° < 2\theta < 34°$ enlargement of XRPD pattern shown in a) highlighting the 2θ-shift of the most intense peak; b) XPS Pt 4f spectrum of as prepared LSFPt; c) XPS Fe 2p spectra of as prepared LSF and LSFPt; d) weight loss (%) vs. temperature for as prepared LSF, and LSFPt between 25 °C and 950 °C in N_2 atmosphere; e) O_2-TPD profiles of as prepared LSF, and LSFPt between 25 °C and 850 °C.

Table 1
Relative concentrations of iron obtained fitting the Fe 2p spectra reported in Fig. 1c.

Sample	Fe^{3+} (%)	Fe^{4+}(%)	Fe^{4+}/Fe^{3+}
LSF	67.9	32.1	0.47
LSFPt	56.2	43.8	0.78

easily discriminated, thus Fe^{2+} was not included in Table 1.

Fe^{3+} relative concentration decreased from 67.9% in LSF to 56.2% in LSFPt, while the Fe^{4+}-related component raises from 32.1% to 43.8%. Pt inclusion increased the amount of 4 + cations at the B-site and the net effect on the perovskite lattice was a larger oxygen retention capacity, to ensure the overall electroneutrality.

Fig. 1d shows the TG profiles of LSF and LSFPt samples from room temperature to 950 °C recorded in flowing N_2. For both samples, the weight loss is <2% and it can be ascribed to oxygen being released from the sample due to thermal depletion of oxygen vacancies. At 950 °C the mass losses were 1.15% and 1.71% for LSFPt and LSF, respectively. LSFPt profile shows a lower slope as compared to LSF, especially from room temperature to 200 °C (superficial oxygen release) and at T > 600 °C (lattice oxygen vacancies depletion). O_2-TPD plots of LSFPt and LSF are reported in Fig. 1e. Two main regions can be distinguished, on the basis of the released O_2 (Table 2): the α-region, up to 400 °C, in which low intensity peaks arise from surface and weakly-bound oxygen release, and the β-region, up to 850 °C, that accounts for the majority of oxygen release, likely due to thermally activated oxygen loss from the oxide lattice. Although the oxygen desorption tests were carried out in

Table 2
Oxygen released ($mmol \cdot g^{-1}$) from O_2-TPD analysis for LSFPt and LSF.

	released O_2 ($mmol \cdot g^{-1}$)		
Sample	Low T Peak	High T Peak	Total
LSF	0.057	0.452	0.509
LSFPt	0.047	0.412	0.459

flowing He, a similar trend was observed as the one obtained in the thermogravimetric analysis in N_2 (Fig. 1d), with LSFPt releasing less oxygen as compared to LSF both in the α-region (17.5%) and in the β-region (8.8%). The most intense peak around 600 °C (likely associated to the highest slope of the curves in Fig. 1e) appears shifted from 587 °C for LSF to 685 °C for LSFPt, confirming the larger oxygen retention capacity provided to the oxide structure by the platinum doping. XRPD patterns of both the samples before and after the TG and O_2-TPD analyses were acquired and showed a preserved structural integrity of the samples after the measurements (Fig. S3 in Supplementary Material).

The electrical conductivity of LSF and LSFPt was measured on sintered perovskite samples by DC four-probe method between 300 °C and 850 °C in flowing air. Fig. 2a shows the Arrhenius-like plot and Table 3 reports maximum conductivity (σ_{max}) and activation energy (E_a) values. In Fe-based perovskite oxides, the simultaneous presence of electron holes and oxygen vacancies as charge carriers enables a mixed ionic and electronic conductivity (MIEC). However, the electronic conductivity results 2–3 orders of magnitude larger than the ionic one, thus the former represents the major contribution to DC conductivity [40]. Data in Fig. 2a exhibit the typical trend of LSF-based oxides: *p*-type conduction occurs via thermally activated small polaron hopping through the Fe^{3+}-O-Fe^{4+} paths in the lattice until T ~ 600 °C. At higher temperature, holes are annihilated to compensate for the progressive oxygen loss and the conductivity decreases showing a metal-like trend.

The measured LSF conductivity is in good agreement with previously reported values for the same stoichiometry [41]. Fig. 2a shows that LSFPt data match those of LSF within the experimental error. 5 mol% Pt doping did not significantly affect LSF conductivity, that remained well above the threshold for application as a solid oxide cell air electrode (100 S·cm^{-1}) [42], both in the IT-operational range (600 °C –850 °C) and for lower temperatures. On the other hand, Pt-doping in the perovskite lattice positively affected the activation energy for the polaron hopping mechanism, that decreased by 19% (Table 3). The observed lowering in E_a might arise from the larger availability of Fe^{4+}/Fe^{3+} couples in LSFPt as compared to LSF (Table 1) introduced by Pt-doping: a similar improvement in the polaron hopping mechanism (lower activation energy) was reported as a consequence of Fe^{4+}/Fe^{3+} ratio increase upon B-site substitution in lanthanum strontium ferrites [43].

3.2. Air electrode characterization

LSFPt electrochemical activity as air-electrode was assessed by means of ASR evaluation on LSGM-supported symmetric cells and compared to both the undoped compound (LSF) and to the state-of-the-art 20 mol% Co-substituted lanthanum ferrite, LSCF. EIS data were best fitted with an $R_s(CR)_1(QR)_2(QR)_3$ equivalent circuit, where R is the resistance, C is the capacitance and Q is the constant phase element (CPE), and the obtained parameters are reported in Table S1. Fig. 2b shows the area specific resistance (ASR) of LSFPt, LSF and LSCF in the 550 °C–850 °C temperature range. As expected, LSCF and LSF displayed the lowest and the highest ASR values, respectively, in the whole investigated range. LSFPt showed comparable resistance values to LSF at 550 °C, then approached LSCF performance at temperature higher than 700 °C. Fig. 2c shows the Nyquist plots at 750 °C: the total polarization resistance for undoped LSF was 0.31 Ω·cm^2, the introduction of 5 % mol Pt resulted in a 29% resistance decrease (0.22 Ω·cm^2), close to the 0.21 Ω·cm^2 of LSCF. LSFPt exhibited a higher temperature-dependent behaviour, as confirmed by the highest activation energy value: 1.43 ± 0.03, 1.37 ± 0.02 and 1.31 ± 0.05 eV, for LSFPt, LSF and LSCF, respectively. According to TG and O_2-TPD profiles in Fig. 1d and 1e, the oxygen released above 700 °C allowed for larger oxide ions mobility and the full exploitation of platinum catalytic activity, approaching ASR values close to the ones obtained with 20 mol% Co-substituted LSF.

Table 3
Maximum conductivity values and activation energies for LSF and LSFPt measured in air.

Sample	σ_{max} (S·cm^{-1})	E_a (eV)
LSF	189 ± 7	0.140 ± 0.004
LSFPt	189 ± 10	0.114 ± 0.002

To have a better understanding of how Pt-doping lowered the resistance of oxygen exchange reactions occurring at LSF electrode, impedance spectra of LSFPt/LSGM/LSFPt and LSF/LSGM/LSF cells were recorded at different oxygen partial pressures, between 0.21 atm and 0.01 atm, fixing the temperature at 750 °C. Again, the results were compared to an LSCF/LSGM/LSCF cell, tested in identical conditions. DRT analysis was carried out on EIS data and profiles are shown in Fig. 3a, 3b, and 3c for LSF, LSFPt and LSCF, respectively.

As expected, for all samples the decrease in pO_2 led to a progressive resistance increment. DRT spectra show three main peaks (P_{HF}, P_{MF}, P_{LF}) corresponding to the reaction stages occurring at different frequencies: 10^3-10^2 Hz (High Frequency), 10^2-10^0 Hz (Medium Frequency) and 10^0-10^{-1} Hz (Low Frequency). The impedance contributions (areas of separated peaks) will be addressed as R_{HF}, R_{MF}, R_{LF} in the following. For all compounds, P_{HF} accounted for the lowest intensity and did not show significant dependence on pO_2 variation, thus R_{HF} can be related to O^{2-} transfer at the electrode/electrolyte interface [44]. Conversely, P_{MF} and P_{LF} were strongly dependent on pO_2: both peaks increased and shifted toward lower frequency with the decrease of the oxygen partial pressure. Fig. 3a–c clearly show that medium-frequency processes represented the reaction rate determining steps for the three samples, followed by the low-frequency steps. The relation between polarization resistance (R_{pol}) and pO_2 has been investigated to unveil ORR mechanisms on SOFC cathode materials and it is as follows [45,46]:

$$R_{pol}^{-1} \propto k \cdot pO_2^{\,n} \quad (1)$$

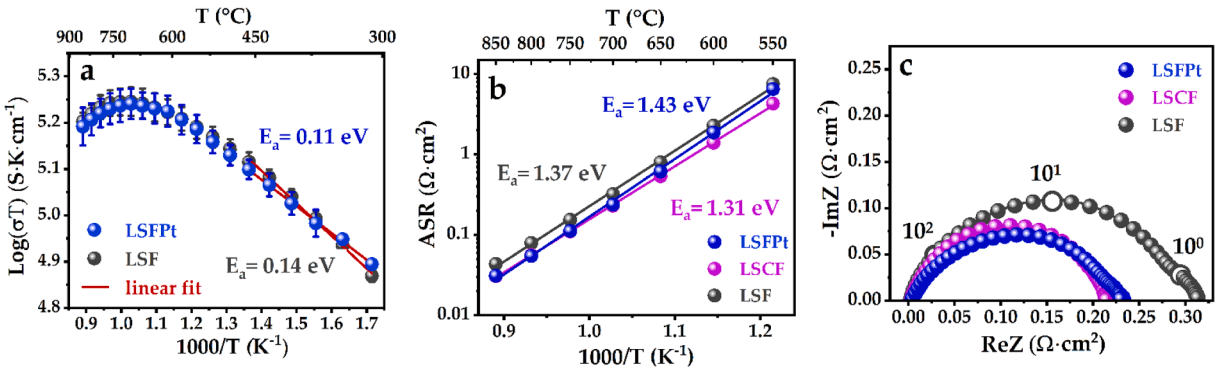

Fig. 2. a) LSF and LSFPt conductivity Arrhenius-like plots: log(σT) vs 1000/T; b) ASR for LSFPt, LSF and LSCF vs 1000/T in air between 550 and 850 °C; c) Nyquist plot at 750 °C for LSFPt, LSF and LSCF.

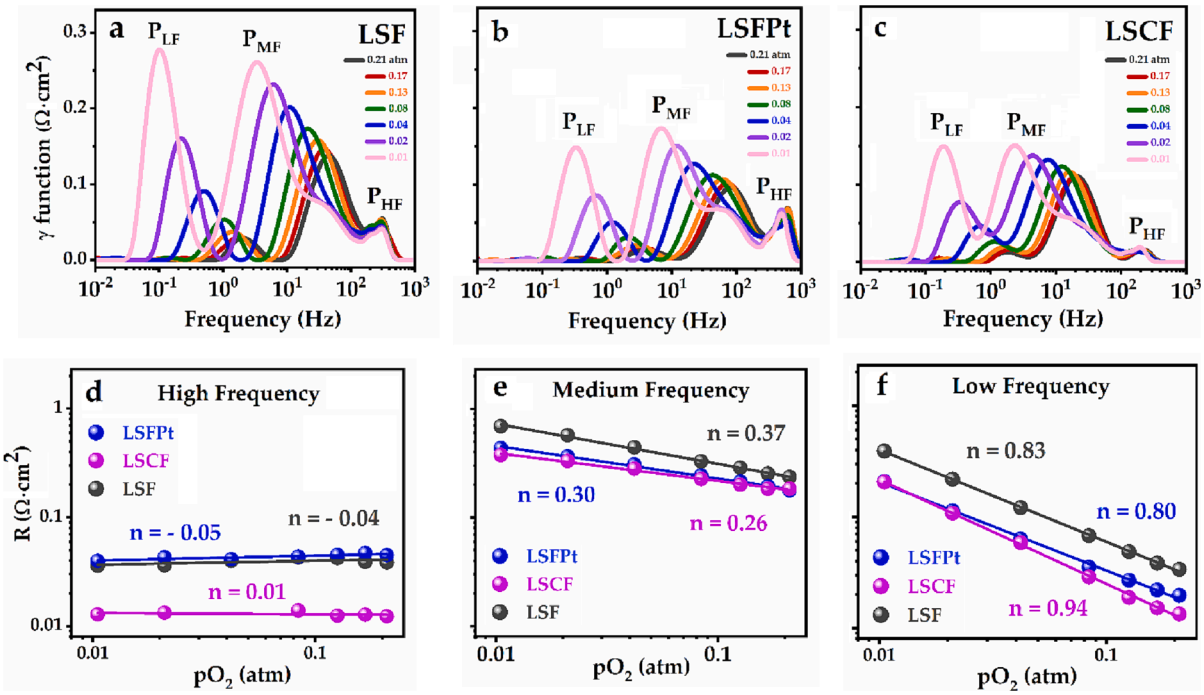

Fig. 3. DRT plots obtained from EIS analyses at 750 °C in different pO_2 for LSF a), LSFPt b) and LSCF c), respectively; R vs pO_2 plots for d) HF, e) MF and f) LF respectively.

where k is pO_2 independent, while n ranges from 1 to 0, according to the oxygen reduction reaction step and the species involved. When $n \sim 1$ the limiting step is represented by molecular oxygen diffusion at the electrode surface,

$$O_2(g) \rightarrow O_2(ad) \quad (2)$$

intermediate n values, like 0.5 and 0.25, denote highly resistive molecular oxygen dissociation with consequent atomic diffusion inside the electrode (3) and charge transfer (4), respectively.

$$O_2(ad) \rightarrow 2O(ad) \quad (3)$$

$$O(ad) + 2e^{'} + V_O^{\cdot\cdot} \rightarrow O_O^x \quad (4)$$

Finally when n approaches 0 the RDS is less dependent from pO_2 variations and involves O^{2-} transfer along the electrode/electrolyte interface:

$$O^{2-}_{electrode} \rightarrow O^{2-}_{electrolyte} \quad (5)$$

The measured trends of R_{HF}, R_{MF} and R_{LF} vs. pO_2 for LSF, LSFPt and LSCF are displayed in Fig. 3d–f and the n-values for the different compounds are shown in Table 4. From the DRT profiles of Fig. 3a–c it is clear that the rate determining step occurs in the medium frequency range, especially for higher pO_2 values, thus close to operating conditions. Here, the reference LSCF shows $n = 0.26$, revealing a purely charge transfer-dominated rate determining step. On the other hand, $n = 0.37$ in LSF reveals that sluggish O_2 adsorption and dissociation represent a limiting factor. This latter aspect was in fact indicated as the RDS for $La_{1-x}Sr_xFeO_{3-\delta}$ family of perovskite oxides [46]. In this respect, 5 mol% Pt-doping ($n = 0.30$) lowered the resistance for O_2 adsorption and dissociation, shifting the RDS towards a charge-transfer-limited reaction.

Table 4
n-values of R_{HF}, R_{MF} and R_{LF} vs pO_2 trend for LSF, LSFPt and LSCF.

Sample	n-value (HF)	n-value (MF)	n-value (LF)
LSF	−0.04 ± 0.02	0.37 ± 0.01	0.83 ± 0.01
LSFPt	−0.05 ± 0.01	0.30 ± 0.01	0.80 ± 0.02
LSCF	0.01 ± 0.02	0.26 ± 0.01	0.94 ± 0.02

To evaluate how Pt-doping affected the perovskite capability of oxygen species adsorption, XPS O 1 s spectra of LSF and LSFPt were acquired before and after an oxygen plasma treatment. Results are reported in Fig. 4 and Table S2.

O 1 s signals in Fig. 4 show two main features, a low B.E. component, O_I (528–530 eV) typically assigned to strongly bound O^{2-} species, thus lattice oxygen, and O_{II} (531–534 eV) commonly related to surface adsorbed oxygen species, such as OH^-/O_2, including physically adsorbed H_2O [36,47]. The most intense component in the as-prepared samples is O_I. A small contribution at lower B.E. is present in LSFPt, likely due to Pt-O bonds in the perovskite lattice [27]. After the activation of the perovskite surface due to the sample exposure to oxygen plasma, O_{II} increased for both LSF and LSFPt, becoming the major contribution to the whole signal (Fig. 4 b-d). The treatment dramatically increased O_{II} for LSFPt as compared to LSF. Pt-doping enhanced the ability to adsorb oxygen: as shown in Fig. 1e, at operating temperatures (T > 650 °C) adsorbed oxygen is thermally released, increasing the electrochemically active sites for SOC air-electrode reactions.

3.3. Fuel electrode characterization

To evaluate the applicability of LSFPt as electrode of symmetric devices, the structural evolution in reducing environments typical of the fuel electrode compartment was investigated. Fig. 5a shows the H_2-TPR profiles of LSF and LSFPt from RT to 1000 °C, while the H_2 consumption is reported in Table 5. Since La and Sr cations are not reducible under the reported experimental conditions, the displayed hydrogen consumption can be entirely attributed to the reduction of B-site cations. LSF profile shows two main features: a first peak around 315 °C and a second broad peak between 700 °C and 1000 °C. The lower temperature hydrogen consumption is generally attributed to $Fe^{4+} \rightarrow Fe^{3+}$ reduction, while $Fe^{3+} \rightarrow Fe^{2+}$ and $Fe^{2+} \rightarrow Fe^0$ begin above 700 °C and eventually lead to metallic iron segregation along with the oxide substrate collapse [48]. Pt-doping markedly modified the H_2-TPR profile: the sharp peak at

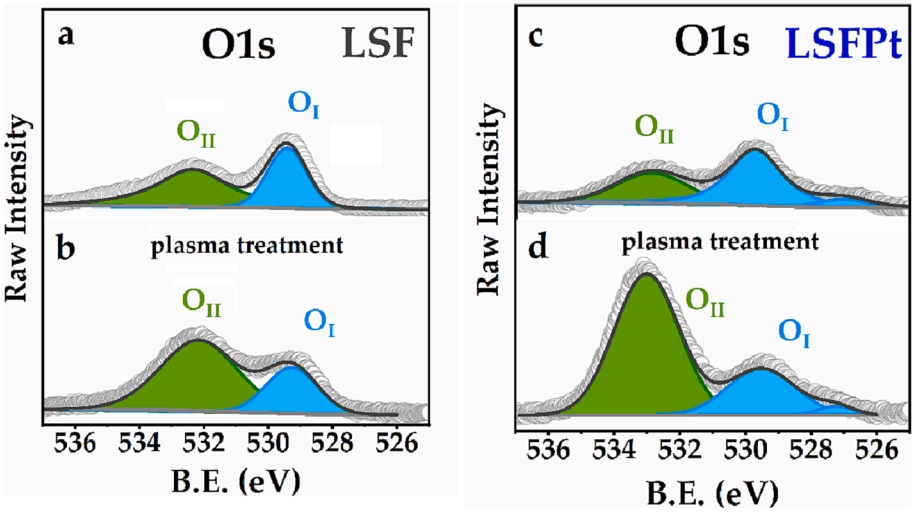

Fig. 4. XPS O 1 s spectra of a), as-prepared LSF; b) LSF after oxygen plasma treatment; c) as-prepared LSFPt; d) LSFPt after oxygen plasma treatment.

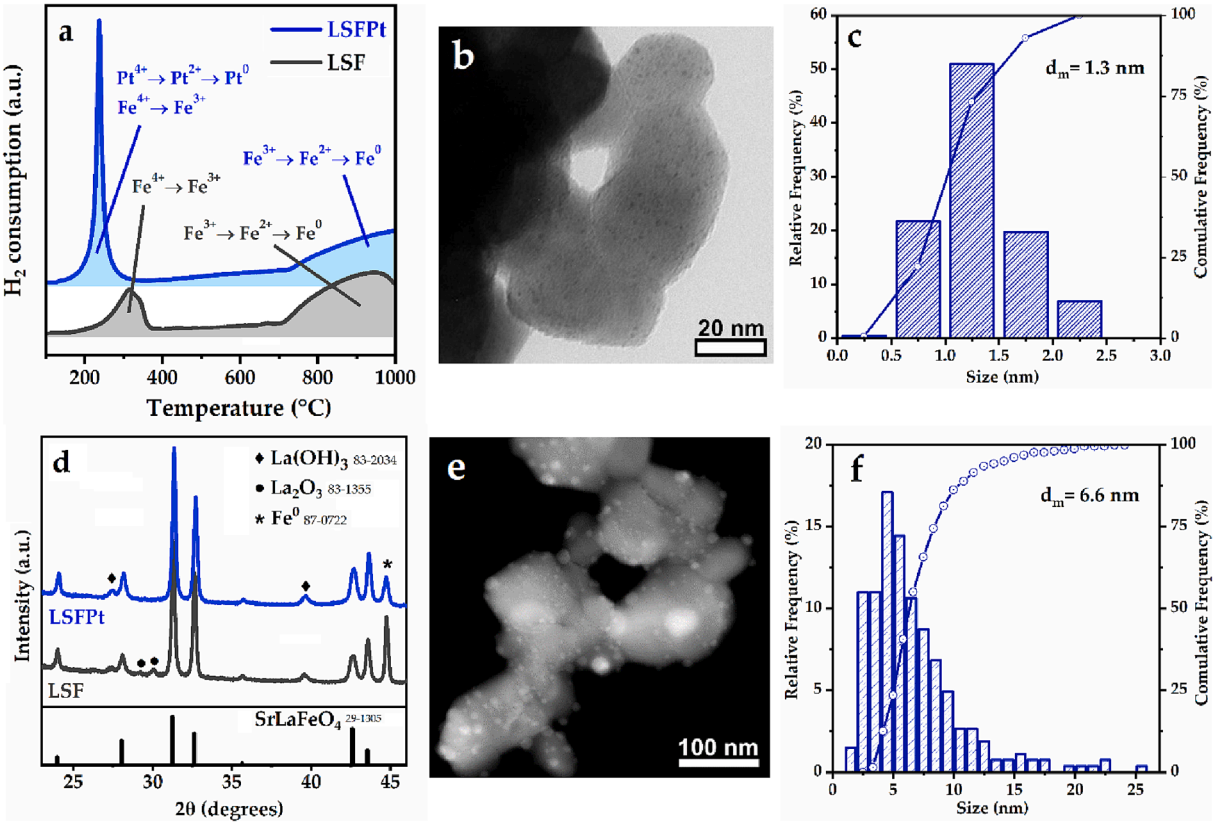

Fig. 5. a) H_2-TPR patterns of LSF and LSFPt; b) Representative TEM micrograph of LSFPt treated for 10 h at 500 °C under flowing 5% H_2/Ar, and c) related size distribution of exsolved NPs; d) XRPD profiles of LSF and LSFPt after reduction treatment for 10 h at 750 °C under flowing 5% H_2/Ar; e) Representative STEM micrograph of LSFPt treated for 10 h at 750 °C under flowing 5% H_2/Ar, and f) related size distribution of exsolved NPs;

Table 5
Amount of hydrogen consumption for LSFPt and LSF from H_2-TPR analysis.

	consumed H_2 (mmol·g^{-1})		
Sample	Low T Peak	High T Peak	Total
LSF	0.93	4.41	5.34
LSFPt	1.55	3.63	5.18

238 °C accounts for higher H_2 consumption if compared to the low-T peak in LSF profile, 1.55 mmol·g^{-1} vs. 0.93 mmol·g^{-1}, respectively. This feature in LSFPt likely arises from the overlap of two contributions: $Fe^{4+} \rightarrow Fe^{3+}$ and $Pt^{4+} \rightarrow Pt^0$ reductions. The lower Gibbs free energy of reduction to metal displayed by Pt as compared to Fe [24] is responsible for the −77 °C peak shift with respect to the un-doped LSF: newly formed surface Pt^0 NPs might trigger $Fe^{4+} \rightarrow Fe^{3+}$ through hydrogen spillover [49]. Nevertheless, the total amount of consumed hydrogen is slightly higher for LSF than for LSFPt, due to a higher H_2 intake shown by the undoped perovskite at higher temperatures (Table 5).

According to literature, when heated in H_2, LSF starts segregating metallic iron at temperatures above 450 °C [50]. Here, LSFPt and LSF were treated in 5% H_2/Ar at 500 °C and 750 °C to evaluate Pt-doping impact on B-site metal segregation. The 500 °C and 750 °C reduced samples will be referred to as 500-LSFPt, 500-LSF and 750-LSFPt, 750-LSF, respectively. XRPD profiles of 500-LSFPt and 500-LSF are shown in Fig. S4: after the 10 h treatment, LSF exhibits traces of initial decomposition in form of low intense impurity peaks, while for LSFPt structural integrity was retained. TEM analysis on 500-LSFPt is reported in Fig. 5b: the perovskite grains show an ultra-fine distribution of nanoparticles displaying a very narrow size range between 0.5 nm and 2.3 nm (average diameter = 1.3 nm, Fig. 5c). SEM images on the same sample (Fig. S5a) show that these NPs homogenously decorate the surface of perovskite grains. On the other hand, 500-LSF show the presence of bigger (4 ± 1 nm) isolated nanoparticles, mainly nucleated at grain boundaries (Fig. S5b).

Thus in 500-LSFPt, the oxide structural integrity was preserved, along with a ultra-fine distribution of nanoparticles, primarily due to Pt segregation.

XRPD pattern of 750-LSF (Fig. 5d) denoted a structure collapse after reduction, with the formation of the layered perovskite structure $SrLaFeO_4$, along with large domains of segregated metallic iron (intense sharp peak at $2\theta = 44.65°$) and lanthanum oxide phases, specifically $La(OH)_3$ and La_2O_3. SEM micrographs of 750-LSF are reported in Fig. S6, exsolved nanoparticles are absent and the large metallic iron grains are not distinguishable. Conversely, 750-LSFPt XRPD pattern showed less prominent iron segregation, together with the complete absence of La_2O_3, denoting a more gradual and controlled structural transition upon reduction.

The STEM micrograph of 750-LSFPt, reported in Fig. 5e, highlights exsolved nanoparticles with an average diameter of 6.6 nm. The size distribution appears very broad, ranging between 1.6 and 25 nm and larger, but almost 90% of the analysed NPs are below 11 nm and 98% are below 20 nm (Fig. 5f).

An EDX map (Fig. 6) was performed to investigate the elemental spatial distribution. La, Sr and O were mainly localized on the oxide backbone, while Fe and Pt signals are present in the regions where nanoparticles appear, with the latter showing a more localized signal than the former. The nanoparticle line profile of Fig. 6 confirms that exsolved NPs are made up of a Pt-Fe alloy (see also Fig. S7a). Likely, Pt early exsolution served as template for subsequent Fe^0 segregation. Pt was nevertheless found also within the substrate (Fig. S7b). Notably, LSFPt exsolution and phase transition are fully reversible over re-oxidation at 750 °C for 10 h as shown in Fig. S8.

3.4. Cell tests

LSFPt-symmetric cells were tested as H_2-SOFCs, CO_2-SOECs and r-SOCs in a 50:50 CO_2:CO gas mixture. Fig. 7 displays overall cell performance and long-term stability tests. H_2 was fluxed at the fuel electrode for 2 h at 850 °C to favor Pt-Fe NPs exsolution before testing (Scheme in Fig. 7a). A symmetric LSF/LSGM/LSF cell was tested as a reference. Fig. 7b shows I-V curves and power densities of the LSFPt-based cell working as H_2-SOFC in the IT range (650 °C – 850 °C). The maximum power densities (MPD), the open-circuit voltage (OCV) values together with cell polarization resistances (R_{pol}) at 650 °C, 750 °C and 850 °C are listed in Table 6, while OCV Nyquist plots at 850 °C are reported in Supplementary Material (Fig. S9). Fig. 7c displays the obtained MPD compared with those of the reference cell (I-V curves and power densities of the LSF reference cell are shown in Fig. S10). Although at 650 °C LSFPt and LSF cell performance are comparable, a noticeable improvement is observed on LSFPt-cell at higher temperatures, with

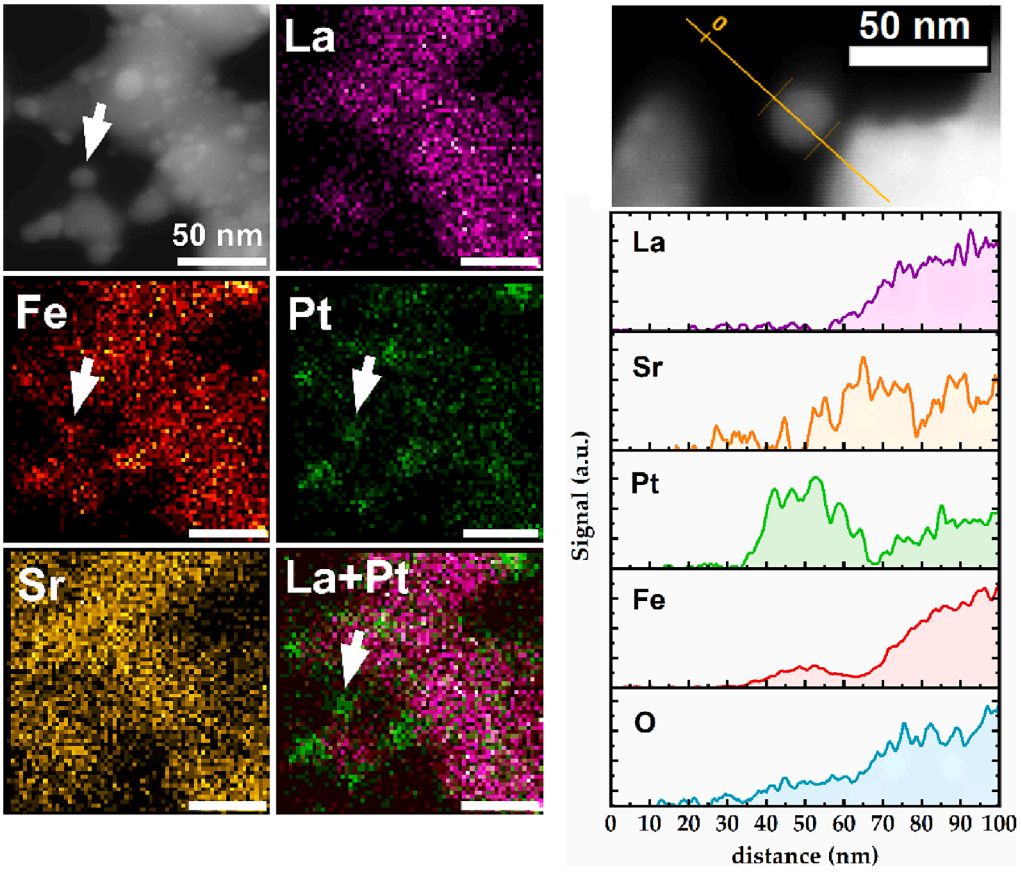

Fig. 6. Left: STEM-EDX elemental map of 750 °C-reduced LSFPt. Arrows help to track the Pt-Fe/enriched exsolved NPs. Right: STEM micrograph and EDX elemental line profile (normalized values) of a representative exsolved particle of 750-LSFPt.

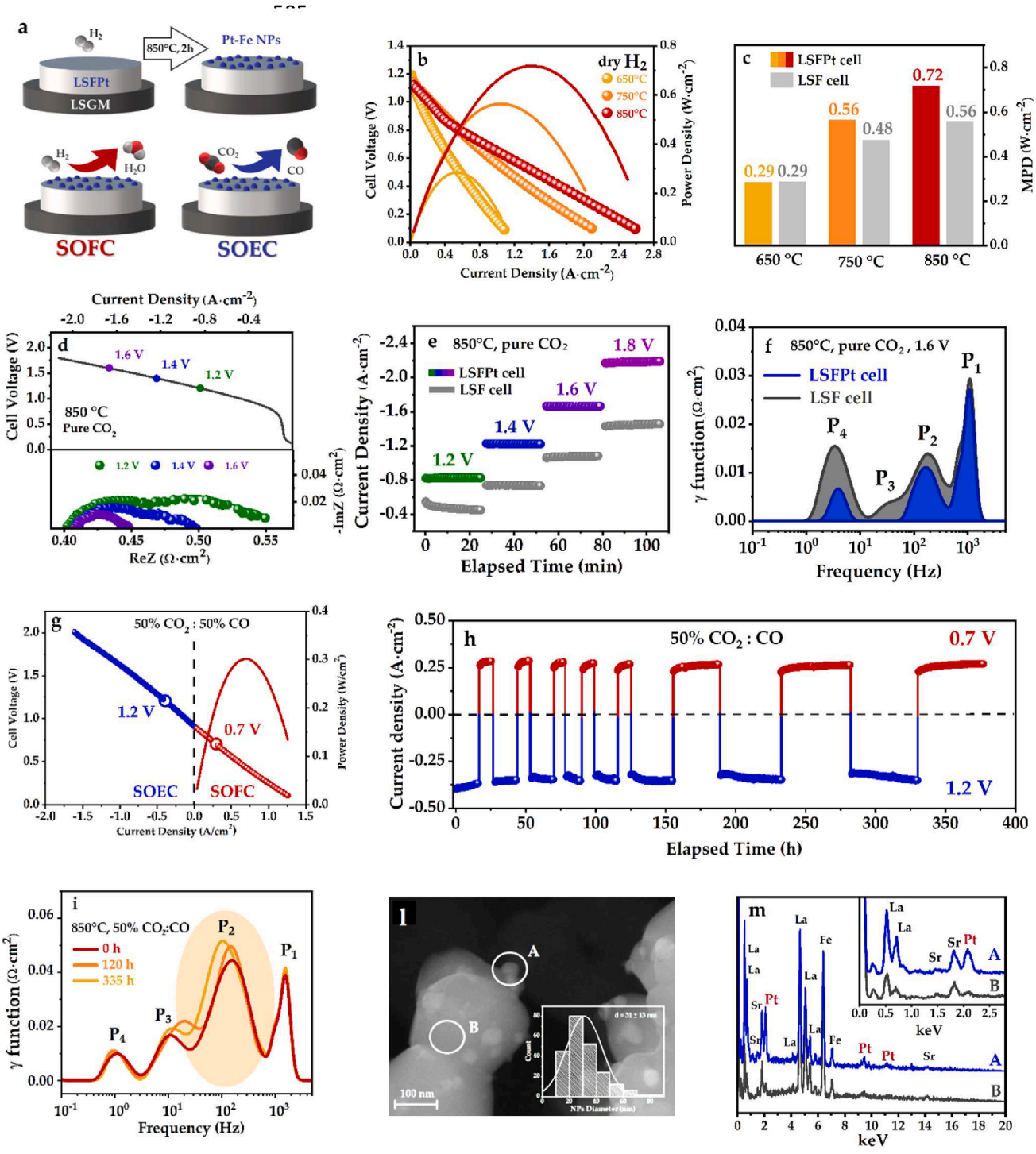

Fig. 7. a) Schematization of the LSFPt-based fuel electrode conditioning prior to the different SSOC tests; b) H_2-SOFC I-V power density curves (650 °C – 850 °C); c) MPD at 650 °C, 750 °C and 850 °C compared to LSF-based cell; d) top: CO_2-SOEC characterization in pure CO_2 at 850 °C, bottom: Nyquist plots of the polarized cell at 1.2 V, 1.4 V, 1.6 V; e) SOEC short-term stability test at 850 °C in pure CO_2, comparison between LSFPt and LSF-based cells; f) LSFPt and LSF-based cells DRT spectra comparison of EIS data in SOEC mode at 1.6 V and 850 °C; g) r-SSOC complete I-V characteristic in 50:50 CO_2:CO at 850 °C; h) reversibility and durability r-SSOC test of LSFPt/LSGM/LSFPt in 50:50 CO_2:CO at 850 °C: the cell was subjected to 0.7 V and 1.2 V polarizations for SOFC and SOEC operations, respectively; i) DRT plots recorded at 0 h, 120 h and 335 h during the endurance test of h); l) SEM micrograph and m) EDX analyses of the spent electrode.

17% and 28% higher MPD at 750 °C and 850 °C, respectively. This improvement reflects the trend observed for the air electrode characterization of Fig. 2b, i.e. the thermal activation of the ORR due to Pt-doping.

CO_2-SOEC tests were carried out at 850 °C in 100 $cm^3 \cdot min^{-1}$ CO_2. The I-V curve from OCV to 1.8 V is shown in Fig. 7d. The potential window was kept below 1.8 V not to trigger gallium reduction in LSGM. The obtained OCV (0.09 V) reflected the low pO_2 difference at the opposite cell compartments [51]. The reversible potential resulting when pure CO_2 is fed at the cathode and air at the anode has been recently reported to be 0.36 V at 800 °C [51]. Here, the low current density observed from OCV to 0.3 V in Fig. 7d results from oxygen being

Table 6
Electrochemical performance of LSFPt/LSGM/LSFPt cell operating in SOFC mode in pure H_2.

T (°C)	gas	OCV (V)	MPD ($W \cdot cm^{-2}$)	R_{pol} ($\Omega \cdot cm^2$)
650	pure H_2	1.19	0.285	1.66
750	pure H_2	1.14	0.564	0.68
850	pure H_2	1.12	0.719	0.58

pumped from the cathodic to the anodic side [52]. The current density output due to CO_2 reduction starts around 0.8 V, reaching 1.66 $A \cdot cm^{-2}$ at 1.6 V. In the lower section of Fig. 7d the impedance spectra at different voltages (1.2 V, 1.4 V and 1.6 V) are shown, with a polarization resistance value as low as 0.039 $\Omega \cdot cm^2$ at 1.6 V. The corresponding LSF SOEC characterization is reported in Fig. S11 while in Table S3 the comparison between R_{ohm} and R_{pol} at different SOEC voltages is shown. The current density for LSF was remarkably lower: 1.17 $A \cdot cm^{-2}$ at 1.6 V, with a R_{pol} at 1.6 V of 0.071 $\Omega \cdot cm^2$. Pt-doping increases the current density by 42%, decreasing the electrode polarization resistance by 45%.

A short-term stability test at different cell voltages (1.2 V−1.8 V) was carried out on both LSFPt and LSF cells at 850 °C in pure CO_2 atmosphere, as shown in Fig. 7e. LSF current density output was lower than that observed for LSFPt at all the potential steps. Moreover, when polarized at 1.2 V the reference LSF cell showed a decreasing current density over time. Although Fe-containing perovskites generally display superior performance as fuel electrodes for CO_2-SOEC [53] it was recently reported how metallic iron catalytically active sites can undergo rapid reoxidation, resulting in current density loss [54,55]. Conversely, the presence of Pt seems to prevent this activity degradation.

To clarify the role of Pt in such an improvement of cell performance, EIS spectra recorded at 1.6 V were analyzed through DRT (Fig. 7f). The profiles show four distinguishable peaks (P_1-P_4) ranging from 10^0 to 10^3 Hz. The 45% decrease of total R_{pol} with LSFPt is almost entirely ascribable to a lowered resistance of the low-frequency processes (P_3, P_4). Literature records converge upon attributing P_3 and P_4 to fuel electrode-related processes: CO_2 dissociative adsorption and diffusion, respectively [56]. The first steps of the CO_2 reduction mechanism involve molecular adsorption on the most catalytically active sites, i.e. oxygen vacancies and/or metal surface [51]. The better activity displayed by LSFPt here, is associated to the presence of platinum in the fine and homogeneous distribution of exsolved NPs, occurred during the fuel electrode pre-reduction treatment (Fig. 5d–f and Fig. 6) and missing in reduced LSF. In fact, among all 4d and 5d transition metals, Pt is known for dramatically lowering the CO_2 and CO adsorption energies on oxide substrates [57] and a P_3-P_4 lowering was recently reported upon ex-situ Pt decoration of a Co-containing perovskite-fluorite composite SOEC fuel electrode [58].

Operational SOFC/SOEC reversibility for LSFPt/LSGM/LSFPt was assessed at 850 °C and tested on the long-term. A constant 50% CO_2 − 50% CO inlet was fed at the fuel compartment. The 0.89 V obtained OCV resulted from the presence of CO as a reducing agent at the fuel electrode. The I-V curves in both modes and Nyquist plots of EIS analyses at 0.7 V (fuel cell) and 1.2 V (electrolyser) polarizations are shown in Figs. 7g and Fig. S12a, respectively.

The I-V characteristic is linear in the whole voltage span, a MPD of 0.301 $W \cdot cm^{-2}$ and a current density of 0.97 $A \cdot cm^{-2}$ at 1.6 V were obtained as SOFC and SOEC, respectively. Polarization resistance was larger for CO_2 reduction than for CO oxidation, 0.11 $\Omega \cdot cm^2$ vs 0.06 $\Omega \cdot cm^2$, respectively. Again, from DRT analysis (Fig. S12b) the impedance difference was clearly observed in the molecular adsorption/dissociation stages (lower frequency range): while in SOEC mode CO desorption represented the limiting step [59], SOFC operation benefited from exsolved platinum, as it is an established catalyst for carbon monoxide oxidation reaction. In fact, recently published Pt-free reversible systems with perovskite oxide-based fuel electrodes, tested in CO_2:CO mixtures at 800 °C and 850 °C, showed larger R_{pol} for SOFC as compared to SOEC operations [60,61].

Cell endurance was evaluated monitoring the current density at fixed voltage over SOFC/SOEC cycles of different duration (8 h and 48 h): the cell output vs. time is shown in Fig. 7h. The device showed remarkable stability both in SOFC and SOEC modes with total current density losses of 7% and 13%, respectively, after 377 h. Such losses mainly occurred within the first cycles and are likely associated with perovskite grain growth and minor electrode/electrolyte interface degradation. Fig. 7i shows the evolution of the cell DRT profile derived from EIS spectra at OCV over time (Nyquist plots are reported in Fig. S13). Data are recorded at the beginning of the endurance test, after 120 h, and 335 h. Ohmic and polarization resistance values are reported in Table S4. The former increased by 6% while the latter by 17%. R_{ohm} increase can be attributed to the commercial electrolyte degradation. According to the DRT plots in Fig. 7i P2 was mainly responsible for the overall cell resistance increase, thus implying a slight worsening of the electrolyte/electrode interface and O^{2-} transport within the electrode oxide backbone. On the other hand, NPs size and stability were negligibly affected by the prolonged operation, as shown in SEM-EDX *post-mortem* cell inspection carried out on the spent fuel-electrode and reported in Fig. 7l, m. In Fig. 7l, individual, non-coarsened Pt-Fe nanoparticles, firmly attached to the perovskite substrate are clearly visible, with an average diameter of 31 ± 13 nm. EDX spot investigation of Fig. 7m confirms that the Pt signal increased in intensity when the electron beam was focused on the particles (site A) as opposed to the substrate (site B). The SEM-EDX post-mortem cell characterization confirmed the overall stability of the catalytically active sites, also excluding the presence of carbon residues.

4. Conclusions

B-site 5 mol% Pt-doping proved to be a successful strategy to enhance the electro-catalytic performance of $La_{0.6}Sr_{0.4}FeO_{3-\delta}$ (LSF), rendering LSFPt a promising electrode for symmetric and reversible solid oxide cells (r-SSOCs). Pt^{4+} cations in the host lattice induced a higher Fe^{4+}/Fe^{3+} ratio, providing LSF with larger oxygen retention capacity. Pt-doping did not affect the high LSF electrical conductivity, showing a σ_{max} of 189 $S \cdot cm^{-1}$. Pt inclusion decreased LSF area-specific resistance by 29% at 750 °C, increasing the catalytic activity towards oxygen exchange-related reactions and eventually approaching the reference 20 mol% Co-substituted LSF (LSCF) at 800 °C−850 °C. According to R_{pol} variation vs. pO_2, the presence of platinum cations lowered the resistance of molecular oxygen adsorption on the electrode surface, and this was confirmed acquiring O 1 s XPS signals for LSFPt and LSF before and after a plasma oxygen treatment. After a simulation of SOFC-anode reduction treatment, LSFPt showed a uniform and fine surface coverage of exsolved Pt-Fe nanoparticles, endowing the electrode material with highly catalytically active sites. Symmetric LSFPt/LSGM/LSFPt cells were fabricated and tested for H_2-SOFC operation, obtaining 720 $mW \cdot cm^{-2}$ of power density at 850 °C. The LSFPt-based device was then tested as CO_2-SOEC at 850 °C, displaying a current density output of 1.66 $A \cdot cm^{-2}$ at 1.6 V in pure CO_2, along with a fast and stable output varying the cell voltage from 1.2 V to 1.8 V. Both SOFC and SOEC tests were compared to a reference LSF/LSGM/LSF cell. Finally, the device reversibility was studied in 50:50 CO_2:CO at 850 °C. In this gas mixture a MPD of 301 $mW \cdot cm^{-2}$ and a current density of 0.97 $A \cdot cm^{-2}$ at 1.6 V were observed in fuel cell and electrolyser modes, respectively. The device reversibly operated between 0.7 V (SOFC) and 1.2 V (SOEC) for over 370 h showing remarkable stability, with 6% and 17% increase of ohmic and polarization resistance. A *post-mortem* SEM-EDX analysis showed remarkable stability of the exsolved Pt-Fe NPs at the end of the reversibility/endurance test.

Declaration of Competing Interest

The authors declare that they have no known competing financial interests or personal relationships that could have appeared to influence the work reported in this paper.

Data availability

Data will be made available on request.

Acknowledgments

This work was funded by the FSE-REACT EU Programma Operativo Nazionale Ricerca e Innovazione 2014-2020 (MUR) for the research contract "Towards the energy transition: multifunctional materials for solid oxide reversible cells" CUP E81B21004910005 and POR FESR LAZIO 2014-2020 MARVELOUS (A0375-2020-36494) project and PRIN-2017-Prot.2017FCFYHK_004 project of the Italian Ministry for University and Research (MUR). The authors gratefully acknowledge Cadia D'Ottavi for the technical support.

Appendix A. Supplementary data

Supplementary data to this article can be found online at https://doi.org/10.1016/j.cej.2023.144448.

References

[1] M.B. Mogensen, M. Chen, H.L. Frandsen, C. Graves, J.B. Hansen, K.V. Hansen, A. Hauch, T. Jacobsen, S.H. Jensen, T.L. Skafte, X. Sun, Reversible solid-oxide cells for clean and sustainable energy, Clean Energy 3 (3) (2019) 175–201.
[2] A. Hauch, R. Küngas, P. Blennow, A.B. Hansen, J.B. Hansen, B.V. Mathiesen, M. B. Mogensen, Recent advances in solid oxide cell technology for electrolysis, Science 370 (2020) eaba6118, https://doi.org/10.1126/science.aba6118.
[3] Y. Ji, J. Kilner, M. Carolan, Electrical properties and oxygen diffusion in yttria-stabilised zirconia (YSZ)–La0. 8Sr0. 2MnO3±δ (LSM) composites, Solid State Ion. 176 (2005) 937–943, https://doi.org/10.1016/j.ssi.2004.11.019.
[4] J.T. Irvine, D. Neagu, M.C. Verbraeken, C. Chatzichristodoulou, C. Graves, M. B. Mogensen, Evolution of the electrochemical interface in high-temperature fuel cells and electrolysers, Nature Energy 1 (2016) 1–13, https://doi.org/10.1038/nenergy.2015.14.
[5] D.K. Niakolas, Sulfur poisoning of Ni-based anodes for solid oxide fuel cells in H/C-based fuels, Appl. Catal. A: General 486 (2014) 123–142, https://doi.org/10.1016/j.apcata.2014.08.015.
[6] M. Mogensen, K. Kammer, Conversion of hydrocarbons in solid oxide fuel cells, Annual Rev. Mater. Res. 33 (2003) 321–331, https://doi.org/10.1146/annurev.matsci.33.022802.092713.
[7] V. Duboviks, R. Maher, M. Kishimoto, L. Cohen, N. Brandon, G. Offer, A Raman spectroscopic study of the carbon deposition mechanism on Ni/CGO electrodes during CO/CO 2 electrolysis, Phys. Chem. Chem. Phys. 16 (2014) 13063–13068, https://doi.org/10.1039/C4CP01503G.
[8] J.R. Wilson, W. Kobsiriphat, R. Mendoza, H.-Y. Chen, J.M. Hiller, D.J. Miller, K. Thornton, P.W. Voorhees, S.B. Adler, S.A. Barnett, Three-dimensional reconstruction of a solid-oxide fuel-cell anode, Nat. Mater. 5 (2006) 541–544, https://doi.org/10.1038/nmat1668.
[9] J. Malzbender, R. Steinbrech, Advanced measurement techniques to characterize thermo-mechanical aspects of solid oxide fuel cells, J. Power Sources 173 (2007) 60–67, https://doi.org/10.1016/j.jpowsour.2007.07.072.
[10] A. Marcucci, F. Zurlo, I.N. Sora, I. Luisetto, S. Licoccia, E. Di Bartolomeo, Pd-doped lanthanum ferrites for symmetric solid oxide fuel cells (SSOFCs), Materialia 8 (2019), 100460, https://doi.org/10.1016/j.mtla.2019.100460.
[11] K. Zhu, B. Luo, Z. Liu, X. Wen, Recent advances and prospects of symmetrical solid oxide fuel cells, Ceram. Int. 48 (7) (2022) 8972–8986.
[12] J.C. Ruiz-Morales, D. Marrero-López, J. Canales-Vázquez, J.T. Irvine, Symmetric and reversible solid oxide fuel cells, RSC Adv. 1 (2011) 1403–1414, https://doi.org/10.1039/C1RA00284H.
[13] C. Ni, J. Zhou, Z. Zhang, S. Li, J. Ni, K. Wu, J.T. Irvine, Iron-based electrode materials for solid oxide fuel cells and electrolysers, Energ. Environ. Sci. 14 (2021) 6287–6319, https://doi.org/10.1039/D1EE01420J.
[14] L. Duranti, I. Luisetto, S. Casciardi, C. Del Gaudio, E. Di Bartolomeo, Multi-functional, high-performing fuel electrode for dry methane oxidation and CO2 electrolysis in reversible solid oxide cells, Electrochim. Acta 394 (2021), 139163, https://doi.org/10.1016/j.electacta.2021.139163.
[15] J. Xu, X. Zhou, L.u. Pan, M. Wu, K. Sun, Oxide composite of La0.3Sr0.7Ti0.3Fe0.7O3-δ and CeO2 as an active fuel electrode for reversible solid oxide cells, J. Power Sources 371 (2017) 1–9.
[16] L. Duranti, I. Natali Sora, F. Zurlo, I. Luisetto, S. Licoccia, E. Di Bartolomeo, The role of manganese substitution on the redox behavior of La0.6Sr0.4Fe0.8Mn0.2O3-δ, J. Eur. Ceram. Soc. 40 (12) (2020) 4076–4083.
[17] L. Duranti, I. Luisetto, S. Licoccia, C. Del Gaudio, E. Di Bartolomeo, Electrochemical performance and stability of LSFMn+ NiSDC anode in dry methane, Electrochim. Acta 362 (2020), 137116, https://doi.org/10.1016/j.electacta.2020.137116.
[18] S.P. Jiang, Development of lanthanum strontium cobalt ferrite perovskite electrodes of solid oxide fuel cells-A review, Int. J. Hydrogen Energy 44 (2019) 7448–7493, https://doi.org/10.1016/j.ijhydene.2019.01.212.
[19] F. Zurlo, I.N. Sora, V. Felice, I. Luisetto, C. D'Ottavi, S. Licoccia, E. Di Bartolomeo, Copper-doped lanthanum ferrites for symmetric SOFCs, Acta Mater. 112 (2016) 77–83, https://doi.org/10.1016/j.actamat.2016.04.015.
[20] F. Zurlo, E. Di Bartolomeo, A. D'Epifanio, V. Felice, I.N. Sora, L. Tortora, S. Licoccia, La0. 8Sr0. 2Fe0. 8Cu0. 2O3− δ as "cobalt-free" cathode for La0. 8Sr0. 2Ga0. 8Mg0. 2O3− δ electrolyte, Journal of Power Sources, 271 (2014) 187-194. https://doi.org/10.1016/j.jpowsour.2014.07.183.
[21] S. Van den Brink, R. Kleijn, B. Sprecher, A. Tukker, Identifying supply risks by mapping the cobalt supply chain, Resour. Conserv. Recycl. 156 (2020), 104743, https://doi.org/10.1016/j.resconrec.2020.104743.
[22] S. Karim, Y.-P. Ting, Recycling pathways for platinum group metals from spent automotive catalyst: A review on conventional approaches and bio-processes, Resources, Conservation and Recycling 170 (2021), 105588, https://doi.org/10.1016/j.resconrec.2021.105588.
[23] J. Lobato, M.A. Montiel, R. Granados, S. Díaz-Abad, C. Sáez, C.M. Fernández-Marchante, M.A. Rodrigo, Towards a Circular Economy for Pt Catalysts. Case Study: Pt Recovery from Electrodes for Hydrogen Production, Case Study: Pt Recovery from Electrodes for Hydrogen Production. https://doi.org/10.2139/ssrn.4243127.
[24] D. Neagu, G. Tsekouras, D.N. Miller, H. Ménard, J.T. Irvine, In situ growth of nanoparticles through control of non-stoichiometry, Nat. Chem. 5 (2013) 916–923, https://doi.org/10.1038/nchem.1773.
[25] M. Marasi, L. Duranti, I. Luisetto, E. Fabbri, S. Licoccia, E. Di Bartolomeo, Ru-doped lanthanum ferrite as a stable and versatile electrode for reversible symmetric solid oxide cells (r-SSOCs), J. Power Sources 555 (2023), 232399, https://doi.org/10.1016/j.jpowsour.2022.232399.
[26] M. Marasi, A.P. Panunzi, L. Duranti, N. Lisi, E. Di Bartolomeo, Enhancing oxygen reduction activity and structural stability of La0. 6Sr0. 4FeO3− δ by 1 mol% Pt and Ru B-site doping for application in all-perovskite IT-SOFCs, ACS Applied Energy Materials 5 (3) (2022) 2918–2928.
[27] X. Li, Z. Chen, Y.i. Yang, D. Huan, H. Su, K. Zhu, N. Shi, Z. Qi, X. Zheng, H. Pan, Z. Zhan, C. Xia, R. Peng, S. Wei, Y. Lu, Highly stable and efficient Pt single-atom catalyst for reversible proton-conducting solid oxide cells, Appl Catal B 316 (2022), 121627, https://doi.org/10.1016/j.apcatb.2022.121627.
[28] M. Kothari, Y. Jeon, D.N. Miller, A.E. Pascui, J. Kilmartin, D. Wails, S. Ramos, A. Chadwick, J.T. Irvine, Platinum incorporation into titanate perovskites to deliver emergent active and stable platinum nanoparticles, Nat. Chem. 13 (2021) 677–682, https://doi.org/10.1038/s41557-021-00696-0.
[29] C. Riedl, M. Siebenhofer, A. Nenning, G. Friedbacher, M. Weiss, C. Rameshan, J. Bernardi, A. Limbeck, M. Kubicek, A.K. Opitz, J. Fleig, Performance modulation through selective, homogenous surface doping of lanthanum strontium ferrite electrodes revealed by in situ PLD impedance measurements, J. Mater. Chem. A 10 (6) (2022) 2973–2986.
[30] T.H. Wan, M. Saccoccio, C. Chen, F. Ciucci, Influence of the discretization methods on the distribution of relaxation times deconvolution: implementing radial basis functions with DRTtools, Electrochim. Acta 184 (2015) 483–499, https://doi.org/10.1016/j.electacta.2015.09.097.
[31] R.D. Shannon, Revised effective ionic radii and systematic studies of interatomic distances in halides and chalcogenides, Acta crystallographica section A: crystal physics, diffraction, theoretical and general crystallography, 32 (1976) 751-767. https://doi.org/10.1107/S0567739476001551.
[32] Z. Shao, Q. Shen, H. Ding, Y. Jiang, S. Li, G. Yang, Synthesis, characterization, and methanol steam reforming performance for hydrogen production on perovskite-type oxides SrCo1-xCuxO3-δ, Ceram. Int. 48 (2022) 11836–11848, https://doi.org/10.1016/j.ceramint.2022.01.054.
[33] T. Rajesh, A. Upadhyay, A.K. Sinha, S.K. Deb, R.N. Devi, Effect of Pt incorporation in LaBO3 (B= Mn, Fe, Co) perovskites on water gas shift activity, J. Mol. Catal. A Chem. 395 (2014) 506–513, https://doi.org/10.1016/j.molcata.2014.09.015.
[34] H. Xu, L. Zeng, L. Cui, W. Guo, C. Gong, G. Xue, In-situ generation of platinum nanoparticles on LaCoO3 matrix for soot oxidation, J. Rare Earths 40 (2022) 888–896, https://doi.org/10.1016/j.jre.2021.06.009.
[35] D.J. Deka, S. Gunduz, T. Fitzgerald, J.T. Miller, A.C. Co, U.S. Ozkan, Production of syngas with controllable H2/CO ratio by high temperature co-electrolysis of CO2 and H2O over Ni and Co-doped lanthanum strontium ferrite perovskite cathodes, Appl. Catal. B 248 (2019) 487–503, https://doi.org/10.1016/j.apcatb.2019.02.045.
[36] F. He, J. Chen, S. Liu, Z. Huang, G. Wei, G. Wang, Y. Cao, K. Zhao, La1-xSrxFeO3 perovskite-type oxides for chemical-looping steam methane reforming: Identification of the surface elements and redox cyclic performance, Int. J. Hydrogen Energy 44 (2019) 10265–10276, https://doi.org/10.1016/j.ijhydene.2019.03.002.
[37] L. Reith, J.N. Hausmann, S. Mebs, I. Mondal, H. Dau, M. Driess, P.W. Menezes, In Situ Detection of Iron in Oxidation States ≥ IV in Cobalt-Iron Oxyhydroxide Reconstructed during Oxygen Evolution Reaction, Adv. Energy Mater. 13 (12) (2023) 2203886.

[38] T. Yamashita, P. Hayes, Analysis of XPS spectra of Fe2+ and Fe3+ ions in oxide materials, Appl. Surf. Sci. 254 (2008) 2441–2449, https://doi.org/10.1016/j.apsusc.2007.09.063.
[39] M.C. Biesinger, B.P. Payne, A.P. Grosvenor, L.W. Lau, A.R. Gerson, R.S.C. Smart, Resolving surface chemical states in XPS analysis of first row transition metals, oxides and hydroxides: Cr, Mn, Fe, Co and Ni, Appl. Surf. Sci. 257 (2011) 2717–2730, https://doi.org/10.1016/j.apsusc.2010.10.051.
[40] J.-W. Yin, Y.-M. Yin, J. Lu, C. Zhang, N.Q. Minh, Z.-F. Ma, Structure and properties of novel cobalt-free oxides Nd x Sr1–x Fe0. 8Cu0. 2O3− δ (0.3≤ x≤ 0.7) as cathodes of intermediate temperature solid oxide fuel cells, J. Phys. Chem. C 118 (2014) 13357–13368, https://doi.org/10.1021/jp500371w.
[41] J. Song, D. Ning, H.J. Bouwmeester, Influence of alkaline-earth metal substitution on structure, electrical conductivity and oxygen transport properties of perovskite-type oxides La 0.6 A 0.4 FeO 3− δ (A= Ca, Sr and Ba), PCCP 22 (2020) 11984–11995, https://doi.org/10.1039/D0CP00247J.
[42] T. Kawada, Perovskite oxide for cathode of SOFCs, Perovskite Oxide for Solid Oxide, Fuel Cells (2009) 147–166, https://doi.org/10.1007/978-0-387-77708-5_7.
[43] A. Braun, S. Erat, D. Bayraktar, A. Harvey, T. Graule, Electronic origin of conductivity changes and isothermal expansion of Ta-and Ti-substituted La1/2Sr1/2Fe-oxide in oxidative and reducing atmosphere, Chem. Mater. 24 (2012) 1529–1535, https://doi.org/10.1021/cm300423m.
[44] J.-D. Kim, G.-D. Kim, J.-W. Moon, Y.-I. Park, W.-H. Lee, K. Kobayashi, M. Nagai, C.-E. Kim, Characterization of LSM–YSZ composite electrode by ac impedance spectroscopy, Solid State Ion. 143 (2001) 379–389, https://doi.org/10.1016/S0167-2738(01)00877-3.
[45] M. Escudero, A. Aguadero, J.A. Alonso, L. Daza, A kinetic study of oxygen reduction reaction on La2NiO4 cathodes by means of impedance spectroscopy, J. Electroanal. Chem. 611 (2007) 107–116, https://doi.org/10.1016/j.jelechem.2007.08.006.
[46] Y. Takeda, R. Kanno, M. Noda, Y. Tomida, O. Yamamoto, Cathodic polarization phenomena of perovskite oxide electrodes with stabilized zirconia, J. Electrochem. Soc. 134 (1987) 2656, https://doi.org/10.1149/1.2100267.
[47] D.J. Deka, J. Kim, S. Gunduz, D. Jain, Y. Shi, J.T. Miller, A.C. Co, U.S. Ozkan, Coke formation during high-temperature CO2 electrolysis over AFeO3 (A= La/Sr) cathode: effect of A-site metal segregation, Appl. Catal. B 283 (2021), 119642, https://doi.org/10.1016/j.apcatb.2020.119642.
[48] W. Hernández, M. Tsampas, C. Zhao, A. Boreave, F. Bosselet, P. Vernoux, La/Sr-based perovskites as soot oxidation catalysts for gasoline particulate filters, Catal. Today 258 (2015) 525–534, https://doi.org/10.1016/j.cattod.2014.12.021.
[49] J. Im, H. Shin, H. Jang, H. Kim, M. Choi, Maximizing the catalytic function of hydrogen spillover in platinum-encapsulated aluminosilicates with controlled nanostructures, Nat. Commun. 5 (2014) 3370, https://doi.org/10.1038/ncomms4370.
[50] T. Götsch, L. Schlicker, M.F. Bekheet, A. Doran, M. Grünbacher, C. Praty, M. Tada, H. Matsui, N. Ishiguro, A. Gurlo, B. Klötzer, S. Penner, Structural investigations of La 0.6 Sr 0.4 FeO 3− δ under reducing conditions: kinetic and thermodynamic limitations for phase transformations and iron exsolution phenomena, RSC Adv. 8 (6) (2018) 3120–3131.
[51] Y. Jiang, F. Chen, C. Xia, A review on cathode processes and materials for electro-reduction of carbon dioxide in solid oxide electrolysis cells, J. Power Sources 493 (2021), 229713, https://doi.org/10.1016/j.jpowsour.2021.229713.
[52] Y. Xie, J. Xiao, D. Liu, J. Liu, C. Yang, Electrolysis of carbon dioxide in a solid oxide electrolyzer with silver-gadolinium-doped ceria cathode, J. Electrochem. Soc. 162 (4) (2015) F397–F402.
[53] E. Tezel, A. Whitten, G. Yarema, R. Denecke, J.-S. McEwen, E. Nikolla, Electrochemical reduction of CO2 using solid oxide electrolysis cells: insights into catalysis by nonstoichiometric mixed metal oxides, ACS Catal. 12 (2022) 11456–11471, https://doi.org/10.1021/acscatal.2c03398.
[54] C. Liu, S. Li, J. Gao, L. Bian, Y. Hou, L. Wang, J. Peng, J. Bao, X. Song, S. An, Enhancing CO2 catalytic adsorption on an Fe nanoparticle-decorated LaSrFeO4+ δ cathode for CO2 electrolysis, ACS Appl. Mater. Interfaces 13 (2021) 8229–8238, https://doi.org/10.1021/acsami.0c18997.
[55] J. Carneiro, X.-K. Gu, E. Tezel, E. Nikolla, Electrochemical reduction of CO2 on metal-based cathode electrocatalysts of solid oxide electrolysis cells, Ind. Eng. Chem. Res. 59 (2020) 15884–15893, https://doi.org/10.1021/acs.iecr.0c02773.
[56] J. Liang, M. Han, Different performance and mechanisms of CO2 electrolysis with CO and H2 as protective gases in solid oxide electrolysis cell, Int. J. Hydrogen Energy 47 (2022) 18606–18618, https://doi.org/10.1016/j.ijhydene.2022.04.061.
[57] J.V. Kildgaard, H.A. Hansen, T. Vegge, DFT+ U study of CO2 reduction and CO oxidation on a reconstructed CeO2− x (110) facet, Mater. Today Adv. 8 (2020), 100111, https://doi.org/10.1016/j.mtadv.2020.100111.
[58] W. Feng, Y. Song, X. Zhang, H. Lv, Q. Liu, G. Wang, X. Bao, Platinum-decorated ceria enhances CO2 electroreduction in solid oxide electrolysis cells, ChemSusChem 13 (2020) 6290–6295, https://doi.org/10.1002/cssc.202001002.
[59] E.M. Sala, N. Mazzanti, M.B. Mogensen, C. Chatzichristodoulou, Current understanding of ceria surfaces for CO2 reduction in SOECs and future prospects–A review, Solid State Ion. 375 (2022), 115833, https://doi.org/10.1016/j.ssi.2021.115833.
[60] P. Addo, B. Molero-Sanchez, M. Chen, S. Paulson, V. Birss, CO/CO2 study of high performance La0. 3Sr0. 7Fe0. 7Cr0. 3O3–δ reversible SOFC electrodes, Fuel cells, 15 (2015) 689-696. https://doi.org/10.1002/fuce.201400196.
[61] L. Duranti, I. Luisetto, S. Licoccia, C. D'Ottavi, E. Di Bartolomeo, Novel composite fuel electrode for CO2/CO-RSOCs, J. Electrochem. Soc. 168 (10) (2021), 104507, https://doi.org/10.1149/1945-7111/ac2c15.